

A search for cosmic topology in the final WMAP data

R. Aurich and S. Lustig

*Institut für Theoretische Physik, Universität Ulm,
Albert-Einstein-Allee 11,
D-89069 Ulm, Germany*

ABSTRACT

A search for matched circle pairs of similar temperature fluctuations in the final WMAP 9yr data is carried out. Such a signature is expected if the space of the Universe is multi-connected. We investigate the relation between the pixel resolution of CMB maps and a Gaussian smoothing in order to lower the probability for missing matched circle pairs. CMB maps having the 3-torus topology are generated with the characteristics of the WMAP satellite in order to determine how large the smoothing should be chosen in CMB maps disturbed by detector noise. The V and W band data are analysed with respect to matched circle pairs and a tentatively signal is found for a circle pair, which lies, however, close to the plane of the Galaxy. It is, however, inconclusive whether this signal is generated by chance, is due to residual foregrounds contained in the V and W band maps, or is due to a genuine topology.

Key words: Cosmology: cosmic microwave background, large-scale structure of Universe

1 INTRODUCTION

Since the cosmic microwave background (CMB) radiation provides us with the earliest admissible electromagnetic radiation, it contains information about the largest scales of our Universe. Therefore, it is most promising to search for topological signatures in the CMB radiation in order to reveal the topology of our Universe. One of the topological tests is the matched circle test proposed by Cornish et al. (1998) on which this paper puts its focus. For an introduction into the topic of cosmic topology and discussions concerning topological tests, see Lachièze-Rey and Luminet (1995); Luminet and Roukema (1999); Levin (2002); Rebouças and Gomero (2004); Luminet (2008); Mota et al. (2010, 2011); Fujii and Yoshii (2011).

The idea behind this test is the following. The CMB sky observed from a given observer position originates from a sphere around this observer, i. e. from the surface of last scattering (SLS). If the Universe possesses a non-trivial topology, the space can be viewed as being tessellated by cells which have to be identified. This space is the so-called universal cover. Each cell has a “clone” of the observer, which observes the same CMB sky. If the observer and a given clone are not farther separated than the diameter of the surface of last scattering, the two spheres overlap in the universal cover. The intersection of the two spheres is a circle seen by the observer and its clone in a different direction. Since the observer and its clone are to be identified, one concludes that two circles should exist on the CMB sky with identical temperature fluctuations seen in different directions but with

the same radius. A non-trivial topology is thus betrayed by as much pairs of circles with the same temperature fluctuations as there are clones of the observer not farther away than the diameter of the surface of last scattering.

This description is simplified since it ignores several effects which alter the CMB temperature fluctuations of the observer and its clone in a different way, so that the temperature fluctuations on both circles are no longer identical. The two most important CMB contributions in this respect are the Doppler contribution, whose magnitude depends on the velocity projection towards the observer, and the integrated Sachs-Wolfe (ISW) contribution, which arises along the path from the surface of last scattering to the observer or to the clone. These two paths are not identified and lead to different contributions to the total CMB signal. These issues are discussed in more detail by Aurich et al. (2006); Riazuelo et al. (2006); Key et al. (2007); Bielewicz and Banday (2011). There are further degrading effects, e. g. the finite thickness of the surface of last scattering, but these are considered as subdominant to the Doppler and ISW contribution. Despite these degrading effects, there should be a detectable topological signal.

In addition to these contributions, which can be computed with the standard CMB physics, there are residuals left over by the subtraction of foreground sources which have their own uncertainties.

The circles-in-the-sky (CITS) test requires a full sky survey and has been applied to different sky maps derived from the WMAP mission. Cornish et al. (2004) and Key et al. (2007) analyse the first year CMB data with re-

spect to nearly back-to-back circle pairs with a negative result. A hint of the Poincaré dodecahedral topology is found by Roukema et al. (2004) in the first year data. The circle signals correspond to circles with a small radius of about 11° . This claim could not be confirmed by Key et al. (2007). The analysis of Aurich et al. (2006) uses a weight function constructed to suppress the Doppler and ISW contributions. It does not find a convincing signal, and only a marginal hint is found in favour of the Poincaré dodecahedral space. The three year WMAP data are investigated with respect to the 3-torus topology by Aurich et al. (2008), and it is found that the degree of uncertainties in the CMB map must be significantly below $50\mu\text{K}$ in order to have a realistic chance to discover such a topology. The seven year WMAP data are analysed by Bielewicz and Banday (2011) with respect to back-to-back circle pairs. They rule out topologies having such circle pairs with radii larger than 10° . This work emphasises the presence of residual Galactic foreground emission close to the Galactic plane in the WMAP ILC 7yr map and chooses to use a mask to eliminate this non-CMB contribution. The search for general circle pairs that are not back-to-back is carried out by Vaudrevange et al. (2012). Although some signals are detected, they are ascribed to the residual foreground contained in the ILC map which is used within the WMAP Kp12 sky mask. This analysis concludes that no topological signal is present in the seven year WMAP data with circle radii above 10° . A CITS search for an orbifold line topology is carried out by Rathaus et al. (2013) and a tentative candidate match is found.

Are those topological spaces definitely ruled out by these CMB analyses? In order to exclude or find possible loop holes in the matched circle pair signal, we generate a high resolution CMB sky map for the 3-torus topology which requires a space with zero curvature, i. e. an Euclidean space. This map is analysed with respect to the amplitude of the topological signal.

The 3-torus map is computed using the cosmological parameters of the ΛCDM concordance model which are published by Jarosik et al. (2011) in their Table 8, column “WMAP+BAO+ H_0 ” ($\Omega_{\text{bar}} = 0.0456$, $\Omega_{\text{cdm}} = 0.227$, Hubble constant $h = 0.704$, reionization optical depth $\tau = 0.087$, scalar spectral index $n_s = 0.963$). In the following only the cubic 3-torus is considered where all three topological lengths have the same value L . In units of the Hubble length $L_H = c/H_0$, the chosen side length is $L = 1.5$ in sections 2 to 4. This value is significantly smaller than that obtained from the requirement that the CMB temperature correlations of the model should match the observed correlations. A best fit of the correlations leads to values around $L = 4$, see figure 11 in Aurich and Lustig (2011). It should be noted that this 3-torus topology with $L = 4$ could be detected in future high-redshift galaxy surveys as emphasised by Roukema et al. (2013) which would be independent of the CMB analyses. The reason for the unrealistically small value of $L = 1.5$ is that the CMB anisotropies have to be computed by using the eigenmodes of the 3-torus, and we want to accurately compute the CMB up to the multipole moment C_l with $l_{\text{max}} = 3000$. To achieve this fine-structure for the chosen cosmological parameters, all eigenmodes with a wavenumber k up to $k = 1026$ are included. This means that 61 556 892 different wavenumbers \vec{k} are taken into account. The simulation of a CMB map for $L = 4$ with that

resolution is currently not feasible. However, the amplitude of the signal due to a single pair of matched circles should be independent of the size of the fundamental cell. The size determines, however, the number of matched circle pairs which decreases with increasing size of the 3-torus cell. The cubic torus topology with $L = 4$ possesses six circle pairs with radius $\alpha \simeq 31^\circ$ and three circle pairs with radius $\alpha \simeq 53^\circ$. The total number of circle pairs increases for $L = 1.5$ to 182. Thus, the simulation with $L = 1.5$ has the advantage that there are much more circle pairs to analyse with respect to their discovery probability. For the decision, whether a cell with $L = 4$ is discovered with certainty, one has to take the much smaller number of circle pairs into account. The CMB sky map for the 3-torus with $L = 1.5$ is generated in the HEALPix format (Górski et al. 2005) with a resolution of $N_{\text{side}} = 4096$. This map possesses a pixel size of $51''.5$ which is three times smaller than the resolution of the simulation being of the order $180^\circ/l_{\text{max}} \sim 3'.6$. The following analysis is mainly based on this map. We will also use less accurate $L = 4$ simulations in sections 5 and 6 when the detector noise is taken into account since in that case a lower accuracy of the simulation is sufficient. Furthermore, we restrict us to a search of back-to-back circle pairs.

2 THE CITS AMPLITUDE FOR INDIVIDUAL CIRCLE PAIRS

Let us now turn to the correlation measure used for the detection of CITS signals. The expansion of the temperature $\delta T_i(\phi)$ along a circle in a Fourier series $\delta T_i(\phi) = \sum_m T_{im} e^{im\phi}$, $0 \leq \phi \leq 2\pi$, allows one to define the m -weighted circle signature for two circles i and j having a radius α as (Cornish et al. 2004)

$$S_{ij}(\alpha, \beta) := \frac{2 \sum_m m T_{im} T_{jm}^* e^{im\beta}}{\sum_m m (|T_{im}|^2 + |T_{jm}|^2)} \quad . \quad (1)$$

The angle β takes a possible shift between the two circles into account. A perfect correlation would be revealed by $S_{ij}(\alpha, \beta) = 1$ but due to the degrading Doppler and ISW contributions, the actual value is lower. Then the maximum is taken over all circle pairs and all shift angles β for a fixed circle radius α , i. e.

$$S(\alpha) = \max_{i,j,\beta} S_{ij}(\alpha, \beta) \quad . \quad (2)$$

In the following we restrict this analysis to back-to-back circles which determines the index j as a function of i . Every pixel i of the HEALPix map is treated as a possible centre of a circle in the CITS search.

Even if the correlation $S(\alpha)$ is computed for a CMB map belonging to a model with a simply-connected topology, one obtains non-vanishing correlations by chance. The smaller the rings, the higher is the probability that the temperature fluctuations are accidentally correlated. This leads to a background for $S(\alpha)$, which starts at $S(\alpha) \simeq 1$ for $\alpha = 0$ and declines towards larger radii α , until at $\alpha = 90^\circ$ the pairs are mapped onto each other leading again to $S(\alpha) \simeq 1$. A topology can only be discerned if the CITS correlation due to a matched circle pair is significantly larger than this background.

This background behaviour is shown in figure 1, where

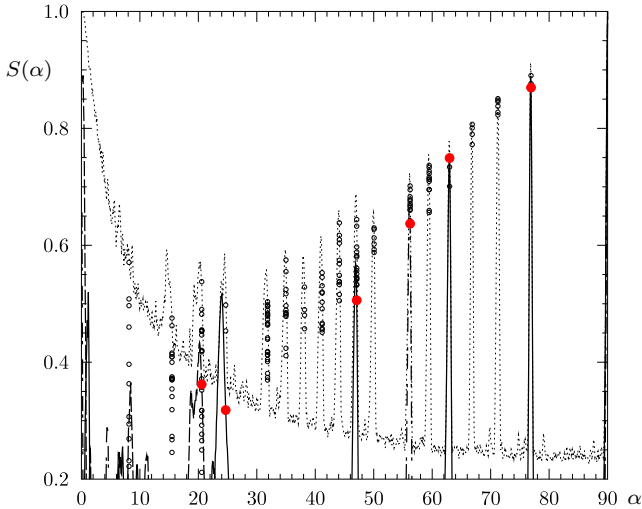


Figure 1. The CITS correlation $S(\alpha)$ is calculated for a 3-torus simulation with $L = 1.5$ using the HEALPix resolution $N_{\text{side}} = 512$ and a Gaussian smoothing with $\theta = 0.5^\circ$. The dotted curve shows $S(\alpha)$ obtained from all back-to-back circle pairs and all shift angles β . The open circles reveal the CITS values obtained from the 182 matched circle pairs of this topology. The dashed, full, and dotted-dashed curves belong to the subset of circle pairs having the same circle centres as one of the matched circle pairs with radii $\alpha = 20.5^\circ$, 24.7° , and 56.2° , respectively. The CITS values of these matched circle pairs are depicted by red dots.

the CITS correlation $S(\alpha)$ is computed from a 3-torus simulation with $L = 1.5$ as described in the Introduction. The dotted curve belongs to $S(\alpha)$ obtained as the maximum taken over all occurring back-to-back circle pairs and all shifts β . Even for very large radii α , the background is not far below 0.3. Since there are 182 matched circle pairs, every peak in $S(\alpha)$ is generated by the circle pair with the highest signal. The figure also reveals the variation in the CITS signal for the individual pairs. For each pair the individual CITS value is depicted by a small circle in figure 1. For $\alpha \lesssim 20^\circ$ the CITS values of matched circle pairs are below the background of non-matched circle pairs, so that such small matched circle pairs can probably not be detected. Above $\alpha \simeq 25^\circ$ the matched circle pairs can be detected under the optimal conditions assumed here, where a pure CMB map without foregrounds and detector noise is available.

The figure 1 also shows the CITS correlation $S(\alpha)$ obtained from the subset of circle pairs having all the same circle centres. For such a subset, the background due to non-matched circle pairs is much lower and not visible in figure 1. The CITS values of three subsets of such circle pairs are plotted with radii $\alpha = 20.5^\circ$, 24.7° , and 56.2° . The CITS values of the matched circle pairs (red dots in figure 1) with $\alpha = 20.5^\circ$ and 24.7° are below the full background (dotted curve). But in their neighbourhood towards smaller radii, there are correlations above the background niveau. This is a numerical observation which is confirmed in many instances: The maximal values in the CITS correlation are not obtained exactly on the matched circle pair, but, instead, for pairs shifted towards smaller radii. This implies

that if one would discover a CITS signal in the real sky map, the radius α of the true circle pair is probably slightly larger than that corresponding to the peak. Along the axis of the selected 24.7° matched circle pair are three further pairs at radii 47.1° , 63.0° , and 76.9° , see the full curve and the corresponding red dots in figure 1. One observes that the shift towards smaller ring radii is less pronounced, if the ring radius α increases.

3 SMOOTHING AND THE CITS AMPLITUDE

Let us now turn to the important question how the smoothing of a CMB map can improve the amplitude of a CITS signal of a matched circle pair so that its peak emerges out of the background. This can be essential for detecting a possible topology. There are several reasons why a smoothing of the map should be carried out. On the one hand, the temperature values of the pixels contain not only the pure CMB signal, but in addition the noise of the detector. Assuming that the noise is independent from pixel to pixel, a smoothing suppresses the noise contribution leading to a cleaner CMB signal. Even without noise a smoothing can be advantageous. Since the data are given on a discretised map, the scan strategy can miss the very localised peaks if the search grid is too coarse. If the data are sufficiently smoothed, even a relatively coarse search grid can find the topological signal, and a lot of computer time can be saved. However, a too strong smoothing will eliminate the CITS signal. Thus there is a relation of how strong the smoothing should be for a given HEALPix resolution N_{side} . As discussed in the Introduction, the CMB signal is composed from different contributions and only the Sachs-Wolfe contribution leads to a clear CITS signal while the Doppler and integrated Sachs-Wolfe contributions deteriorate it. The Sachs-Wolfe contribution provides the largest signal on scales around the first acoustic peak having a scale of roughly 0.8° . Thus the smoothing should at least be smaller than that in order to preserve the information due to the Sachs-Wolfe contribution.

We use a Gaussian smoothing which multiplies the expansion coefficients a_{lm} of the temperature fluctuations $\delta T(\hat{n})$ with respect to spherical harmonics $Y_{lm}(\hat{n})$ by

$$a_{lm}^{\text{sm}} = a_{lm} e^{-\frac{l(l+1)\sigma^2}{2}} \quad \text{with} \quad \sigma = \frac{\pi\theta/180^\circ}{2\sqrt{2\log 2}} \quad , \quad (3)$$

where θ is the smoothing in degrees.

This Gaussian smoothing is applied to the 3-torus simulation with $L = 1.5$. The simulated CMB map is smoothed using the map in the HEALPix resolution $N_{\text{side}} = 4096$. After the Gaussian smoothing, the map is downgraded to $N_{\text{side}} = 256$, and the CITS correlation $S(\alpha)$ is calculated using this $N_{\text{side}} = 256$ map. The result is shown in figure 2, where the smoothing parameters $\theta = 0.1^\circ$, $\theta = 0.4^\circ$, and $\theta = 0.6^\circ$ are used. The panel (a) displays the correlation obtained from the $\theta = 0.1^\circ$ and $\theta = 0.4^\circ$ maps. The background of $S(\alpha)$ increases by increasing the smoothing parameter θ , but on the other hand, also the CITS signal of the matched circle pair increases. In order to decide, whether there is an improvement by increasing θ from $\theta = 0.1^\circ$ to $\theta = 0.4^\circ$, the figure also shows the difference $S_{\theta=0.4^\circ}(\alpha) - S_{\theta=0.1^\circ}(\alpha)$ as a dashed curve. The difference

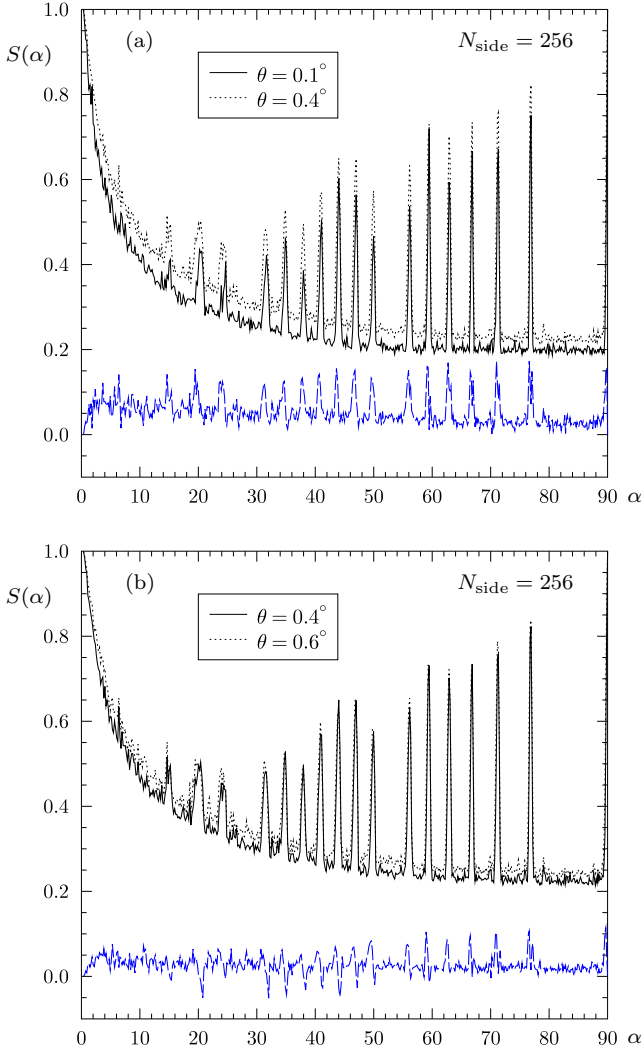


Figure 2. The CITS correlation $S(\alpha)$ is calculated for a 3-torus simulation with $L = 1.5$ using the HEALPix resolution $N_{\text{side}} = 256$ and three different Gaussian smoothing. Panel (a) compares the CITS correlation for the two smoothing parameters $\theta = 0.1^\circ$ and $\theta = 0.4^\circ$, while panel (b) compares $\theta = 0.4^\circ$ and $\theta = 0.6^\circ$. The dashed curve, which starts for $\alpha = 0$ at zero, displays the difference between the two CITS correlations $S(\alpha)$ shown in the panel.

curve reveals the increasing background but also that the peaks are more pronounced for $\theta = 0.4^\circ$, since the peaks are higher than the background. Thus the height of the CITS peaks increases more than the background. Increasing the smoothing further to $\theta = 0.6^\circ$ does not lead to an improvement as shown in panel (b). In panel (b) the difference curve $S_{\theta=0.6^\circ}(\alpha) - S_{\theta=0.4^\circ}(\alpha)$ shows for ring radii $\alpha \lesssim 50^\circ$ dips towards negative values. Thus the increase of the background is larger than the gain in the peak heights. Even for very large rings there is no genuine gain in the height of the peaks, but, instead, they are only extended towards smaller values of α . The focus of the smoothing should be put on the improvement of the signal for medium rings. Therefore, the smoothing parameter θ should be smaller than 0.6° . We

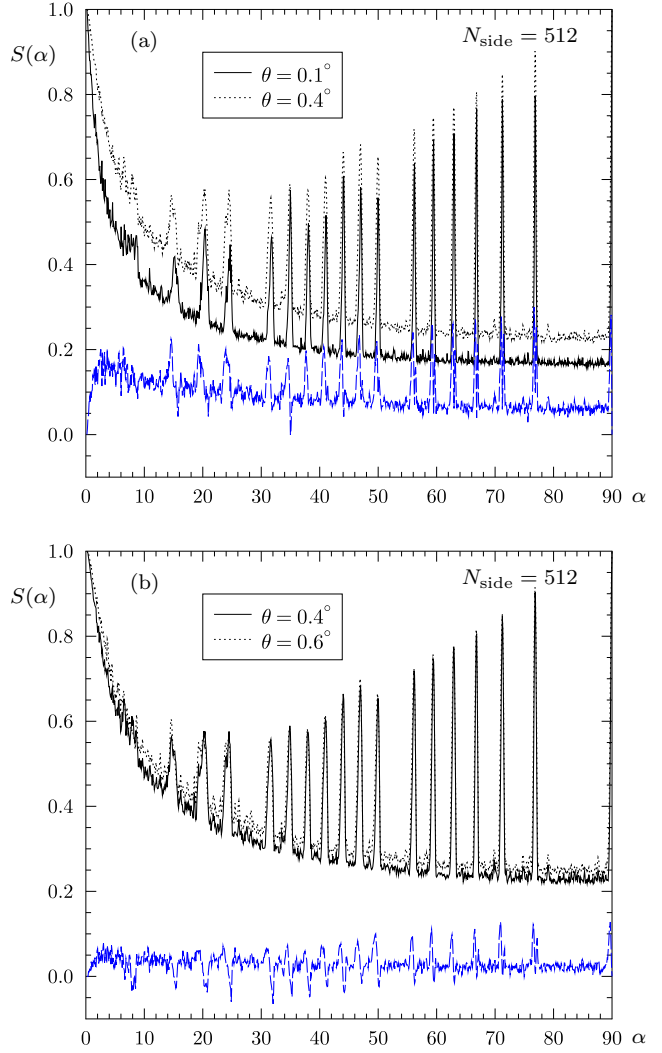


Figure 3. The CITS correlation $S(\alpha)$ is shown for the same simulation as in figure 2 but now calculated from the map in the HEALPix resolution $N_{\text{side}} = 512$. Panel (a) compares the CITS correlation for the two smoothing parameters $\theta = 0.1^\circ$ and $\theta = 0.4^\circ$, while panel (b) compares $\theta = 0.4^\circ$ and $\theta = 0.6^\circ$. The dashed curve, which starts for $\alpha = 0$ at zero, displays the difference between the two CITS correlations $S(\alpha)$ shown in the panel.

have investigated other smoothing parameters θ in this way and conclude that for $N_{\text{side}} = 256$, the best smoothing parameter is about $\theta = 0.4^\circ$.

Let us now address the best choice of the smoothing parameter θ for the HEALPix resolution $N_{\text{side}} = 512$. To that aim, the simulated CMB map is again smoothed using the map in the HEALPix resolution $N_{\text{side}} = 4096$. But after the Gaussian smoothing, the map is only downgraded to $N_{\text{side}} = 512$. The CITS correlation $S(\alpha)$ is calculated from this $N_{\text{side}} = 512$ map and shown in figure 3 in the same way as figure 2 displays the $N_{\text{side}} = 256$ results. Panel (a) shows the increase in the background by increasing the smoothing from $\theta = 0.1^\circ$ to $\theta = 0.4^\circ$, but at least for $\alpha \gtrsim 40^\circ$ the difference curve reveals an improved signal. However, for smaller ring radii the result is inconclusive since positive

as well as negative deviations from the background are observed. This suggests a twofold search if one insists on the $N_{\text{side}} = 512$ resolution: choosing $\theta = 0.4^\circ$ for larger rings and a correspondingly smaller value of θ for smaller rings. The panel (b) shows that a further increase in θ towards $\theta = 0.6^\circ$ does not improve the signal as it was already found in the $N_{\text{side}} = 256$ case.

As a concluding remark of this section, it should be stated that a resolution of $N_{\text{side}} = 128$ should only be used to find matched circle pairs with large radii above $\alpha \gtrsim 40^\circ$. A CITS search should thus be carried out in the $N_{\text{side}} = 256$ resolution using a Gaussian smoothing parameter $\theta = 0.4^\circ$. If the sky map possesses no appreciable noise such that a downgrade to $N_{\text{side}} = 256$ is not necessary as it might be the case for the Planck CMB map, the $N_{\text{side}} = 512$ resolution would be preferable.

4 THE SEARCH GRID

In the CITS search every pixel of the HEALPix map is considered as a possible circle centre of a matched circle pair. The N_{side} resolution leads to $12N_{\text{side}}^2$ pixels and determines how thoroughly the circles are scanned. However, it is not necessary to use for the circle centres, for which the CITS amplitude is to be computed, the same resolution as for the CMB map. Vaudrevange et al. (2012) carry out their CITS search on a CMB map having the resolution $N_{\text{side}} = 512$, but for the circle centres they use the coordinates of the pixel centres of the HEALPix map with the resolution $N_{\text{grid}} = 128$. This procedure saves a lot of computer time since the number of circle centres is reduced by a factor of 16. Except in this section, we always use the same resolution for the search grid and the CMB map.

The coarser search grid harbours the risk that some matched circle pairs get missed. In order to test this issue, we calculate the CITS correlation $S(\alpha)$ from our 3-torus simulation with the HEALPix resolution $N_{\text{side}} = 512$ and a Gaussian smoothing $\theta = 0.4^\circ$. In the first case we use $N_{\text{grid}} = 512$ and search all pixel centres of the $N_{\text{side}} = 512$ map, and in the second case only those of the $N_{\text{grid}} = 128$ mesh. The result can be inferred from figure 4 where the dotted curve shows the $N_{\text{grid}} = 512$ search and the full curve uses the sparse $N_{\text{grid}} = 128$ grid. Several smaller rings are found only on the $N_{\text{grid}} = 512$ grid, see $\alpha = 24.7^\circ$ in figure 4. The CITS correlations for the rings with radii $\alpha = 31.8^\circ$ and $\alpha = 50.0^\circ$ are reduced by a factor of two. Taking into account that our map contains the clean CMB signal without noise and residual foregrounds, it seems that also these signatures can be overlooked. Furthermore, if the multi-connected space has significantly fewer matched circle pairs as it is the case for the $L = 4$ torus topology (six at $\alpha \simeq 31^\circ$ and three at $\alpha \simeq 53^\circ$) mentioned in the Introduction, even this back-to-back signature can be missed. To emphasise the large number of matched circle pairs in the $L = 1.5$ case, the figure 4 also displays the CITS values at the pixel centres that provide the best match to the circle centres as small disks ($N_{\text{grid}} = 512$) and open squares ($N_{\text{grid}} = 128$). It is obvious that a lot of matched circle pairs for the $N_{\text{grid}} = 128$ search are below the background even for $\alpha \lesssim 50^\circ$. All the open squares below the background level would never be considered as candidates for a possi-

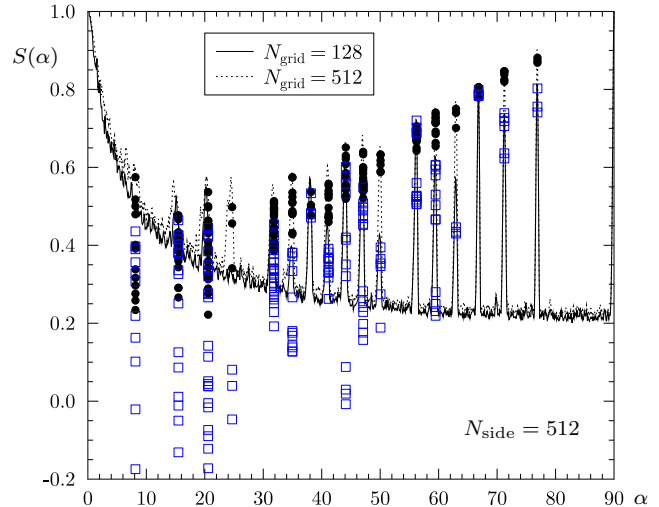


Figure 4. The CITS correlation $S(\alpha)$ is calculated for the 3-torus simulation with $L = 1.5$ using the HEALPix resolution $N_{\text{side}} = 512$ and a Gaussian smoothing $\theta = 0.4^\circ$. The difference in the two curves arises from the resolution N_{grid} of the search grid which provides the coordinates of the circle centres. The dashed curve uses $N_{\text{grid}} = 512$ and the full curve $N_{\text{grid}} = 128$. Note, that both curves are computed from the same $N_{\text{side}} = 512$ CMB map. The values for the individual circle pairs are plotted as small disks ($N_{\text{grid}} = 512$) and open squares ($N_{\text{grid}} = 128$).

ble refined search. Furthermore, since the CITS search of Vaudrevange et al. (2012) refers to non back-to-back circle pairs, their background level is higher than in our back-to-back search. This worsens the situation, so that we doubt that their analysis exclude such matched circle pairs.

Although the computer time would rise dramatically, one could ask how a search grid, which is finer than the resolution of the CMB map, would improve the CITS signature. To address this point, the CITS correlation $S(\alpha)$ is computed for two search grids with $N_{\text{grid}} = 512$ and $N_{\text{grid}} = 1024$ on the 3-torus simulation with the HEALPix resolution $N_{\text{side}} = 512$ and a Gaussian smoothing $\theta = 0.2^\circ$. As figure 5 reveals the improvement justifies the increase in computer time only for small rings with radii $\alpha = 20^\circ \dots 30^\circ$, where the stronger CITS signal is crucial. A similar comparison is carried out for a $N_{\text{side}} = 256$ CMB map, where two search grids with $N_{\text{grid}} = 256$ and $N_{\text{grid}} = 512$ are used. It turns out that only for smoothing parameters θ which are so small that the pixelization determines the resolution of the CMB map, an oversampling with $N_{\text{grid}} > N_{\text{side}}$ leads to significantly better results especially for ring radii in the range $\alpha = 20^\circ \dots 30^\circ$.

5 NOISE AND THE CITS AMPLITUDE

In the previous sections the CITS signature is analysed only for CMB map simulations which contain the pure CMB signal. Only deteriorating effects that have their origin in the CMB physics such as the Doppler and the ISW effect were taken into account. The experiments, in contrast, yield CMB

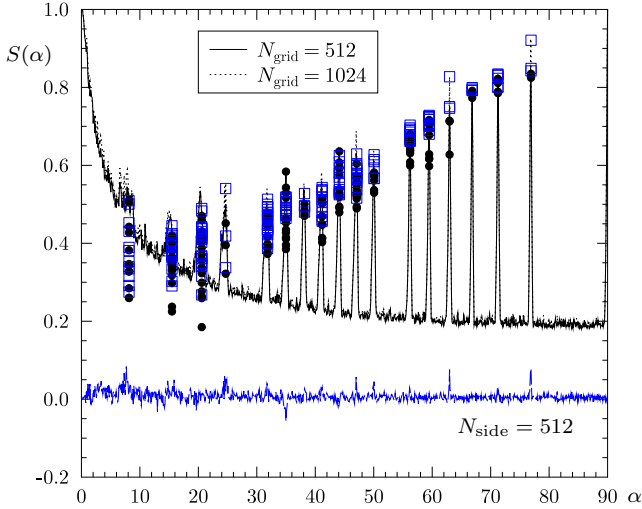


Figure 5. The CITS correlation $S(\alpha)$ is calculated for the 3-torus simulation with $L = 1.5$ using the HEALPix resolution $N_{\text{side}} = 512$ and a Gaussian smoothing $\theta = 0.2^\circ$. The figure shows how the CITS signal improves if a search grid with $N_{\text{grid}} = 1024$ is used on a $N_{\text{side}} = 512$ CMB map. The results for both search grids are shown (full curve for $N_{\text{grid}} = 512$ and dotted curve for $N_{\text{grid}} = 1024$). The values for the individual circle pairs are plotted as small disks ($N_{\text{grid}} = 512$) and open squares ($N_{\text{grid}} = 1024$). The difference curve is also shown, which fluctuates around zero.

maps which are perturbed by noise and the beam profile of the detector.

In order to address that issue, the 3-torus CMB map is modified according to the beam profile $b_{V1,W1}(l)$ of the W1 and V1 channels (Bennett et al. 2012) as given on the LAMBDA website using the HEALPix resolution $N_{\text{side}} = 4096$. Thereafter, a downgrade from $N_{\text{side}} = 4096$ to $N_{\text{side}} = 512$ is carried out. In the next step the noise of the pixel i is computed from the number $N_{\text{obs}}(i)$ of observations of the pixel i as a Gaussian random error with standard deviation $\sigma_0/\sqrt{N_{\text{obs}}(i)}$ and added to the map in the $N_{\text{side}} = 512$ resolution. This map is expanded with respect to a_{lm} and the Gaussian smoothing is realised as

$$a_{lm}^{\text{sm}} = a_{lm} e^{-\frac{l(l+1)\sigma^2}{2}} / b_{V1,W1}(l) \quad , \quad (4)$$

so that the final smoothing is independent of the non-Gaussian beam profile $b(l)$. This sequence of operations leads to CMB maps for the 3-torus topology comparable to the quality of the corresponding WMAP 9yr observations in the V and W bands.

In this section CMB maps for the 3-torus with side length $L = 4.0$ are analysed. In contrast to the $L = 1.5$ simulation, only multipoles l with $l \leq 1000$ are included in the $L = 4.0$ case. This simulation is accurate enough for an analysis with respect to noise as can be inferred from figure 6. For $l > 1000$ the angular power spectrum δT_l^2 is noise dominated for the V and W bands of the WMAP measurements which are put into focus in this section. The comparison of the two panels of figure 6 shows that the W band has a higher noise contribution than the V band, although the

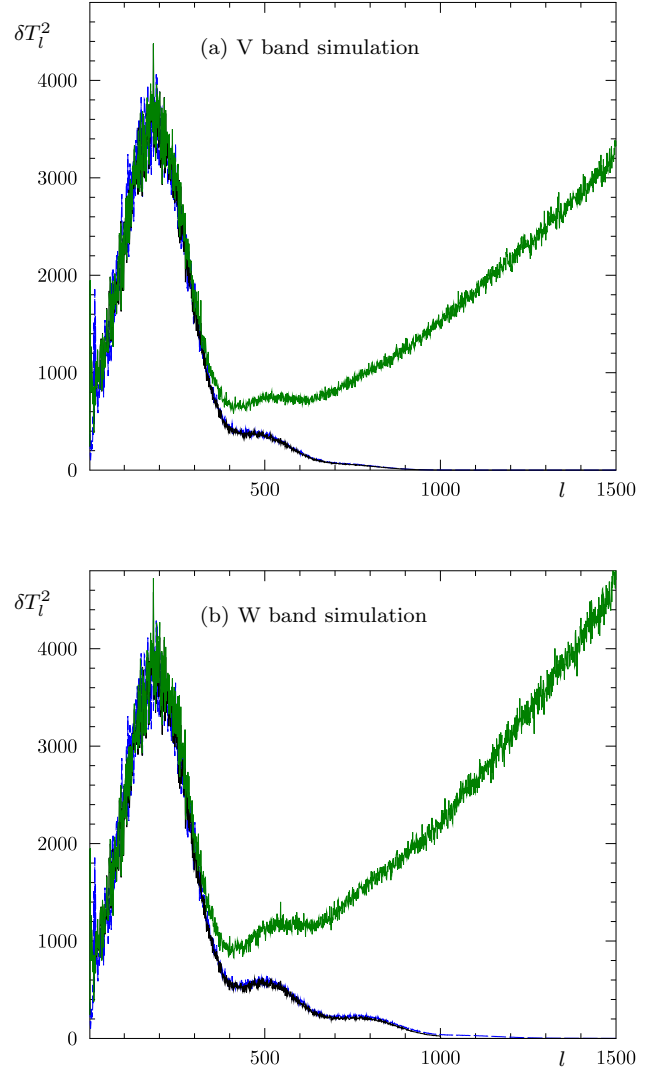


Figure 6. The angular power spectrum $\delta T_l^2 = l(l+1)C_l/(2\pi)$ is shown for two 3-torus simulations with $L = 1.5$ and $L = 4.0$. Two power spectra belonging to $L = 1.5$ and $L = 4.0$ take only the beam profile into account. These two curves are nearly indistinguishable and drop towards zero for large values of l . A marginal difference is visible in the W band simulation for $l > 1000$, where only the $L = 1.5$ simulation has power. Furthermore, the curve increasing for large l belongs to the $L = 4.0$ simulation where in addition to the beam profile also the detector noise is accounted for.

W band beam profile reveals tentatively the third acoustic peak by ignoring the noise.

It is interesting to evaluate the CMB maps, which are processed to mimic the V and W band maps of WMAP, in the $N_{\text{side}} = 512$ resolution without further smoothing. Figure 7 shows that the CITS signature of the 6 ring pairs at $\alpha = 31.1^\circ$ is missing at the $N_{\text{side}} = 512$ resolution in both bands. Only the 3 ring pairs at $\alpha = 52.7^\circ$ emerge slightly from the background, where the signature is more pronounced in the V band having less noise. The CITS signature is swamped by the noise as a simple downgrade to the $N_{\text{side}} = 256$ resolution reveals. Here the average over 4

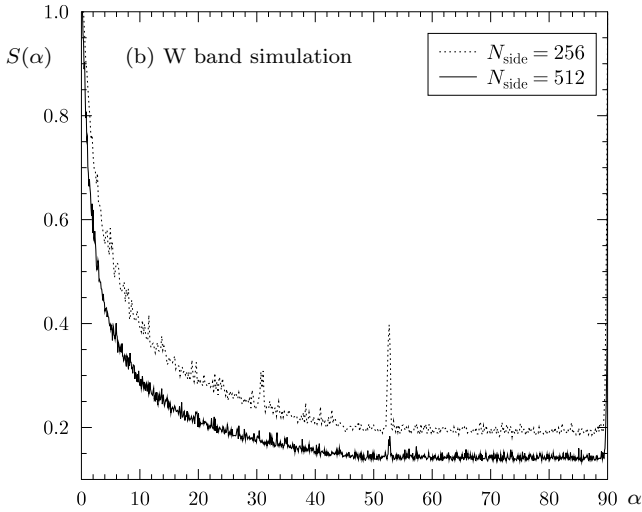
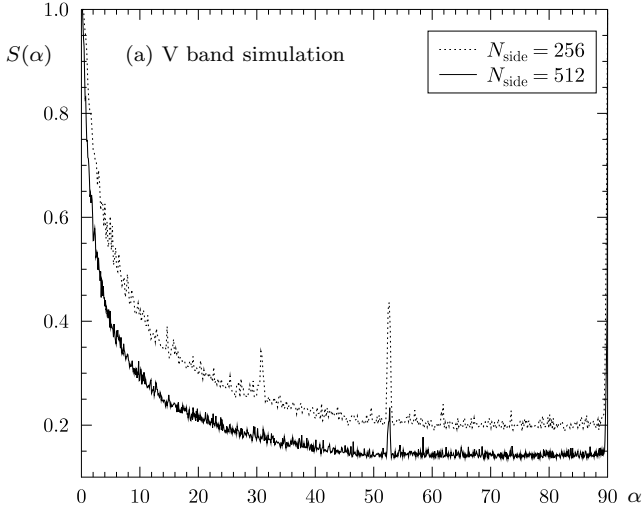


Figure 7. The CITS correlation $S(\alpha)$ is calculated for the 3-torus simulation with $L = 4.0$ using the beam profile and the detector noise of the V band in panel (a) and W band in panel (b). The $N_{\text{side}} = 256$ map is obtained by a downgrade of the $N_{\text{side}} = 512$ map. This topology has 6 ring pairs at $\alpha = 31.1^\circ$ and 3 ring pairs at $\alpha = 52.7^\circ$.

pixels yields the temperature value in the $N_{\text{side}} = 256$ resolution. The improvement can be seen by the dotted curves in figure 7. Despite the increased background, the CITS signature is visible more clearly. This demonstrates that the V and W band CMB maps have to be smoothed in order to reduce the degrading effects due to noise.

The importance of the smoothing to reduce the noise is also revealed by the following analysis. At first the CMB map with the V band properties in the $N_{\text{side}} = 512$ resolution, whose CITS correlation is shown in figure 7(a), is smoothed according to eq.(4). This smoothing is done in the $N_{\text{side}} = 512$ resolution for various values of θ . The optimum is found in the range between $\theta = 0.4^\circ$ and $\theta = 0.5^\circ$. For smoothing parameters θ below $\theta = 0.4^\circ$ the noise degrades the CITS signal and above $\theta = 0.5^\circ$, the smooth-

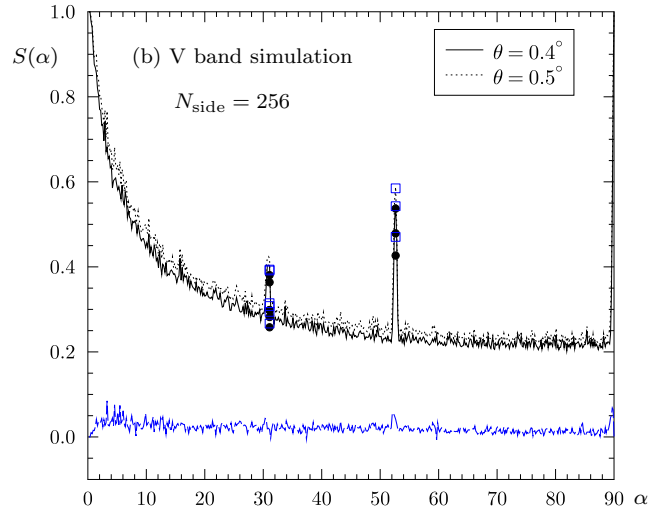
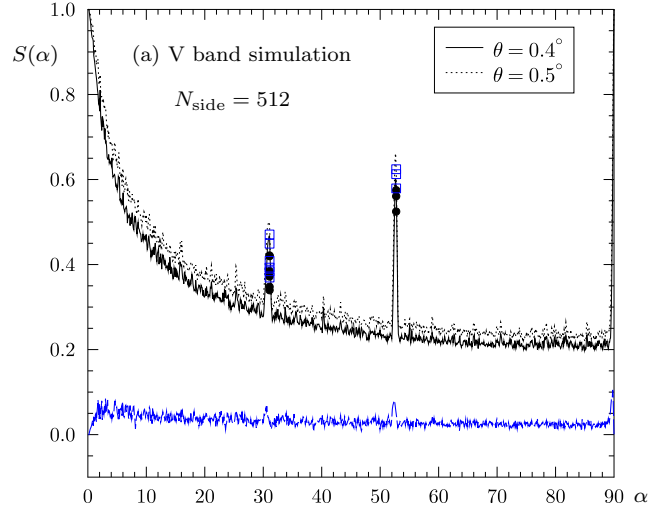


Figure 8. The CITS correlation $S(\alpha)$ is calculated for the 3-torus simulation with $L = 4.0$ using the beam profile and the detector noise of the V band. The CMB map is smoothed using the parameters $\theta = 0.4^\circ$ and $\theta = 0.5^\circ$. In panel (a) $S(\alpha)$ is obtained from the $N_{\text{side}} = 512$ CMB map, while panel (b) shows the corresponding curves obtained from the $N_{\text{side}} = 256$ CMB map. The difference curve is also shown.

ing removes too much CMB information. The CITS correlation is plotted in figure 8(a) for $\theta = 0.4^\circ$ and $\theta = 0.5^\circ$, and the improvement compared to figure 7(a) (full curve) is obvious. In addition, the difference curve is plotted which shows that both smoothing parameters lead to nearly indistinguishable results. In panel (b) of figure 8 the analogous curves are shown for the CMB map which is downgraded to the $N_{\text{side}} = 256$ resolution. Since the computer time is reduced for the smaller $N_{\text{side}} = 256$ resolution, we will use in the following this value of N_{side} .

Up to now the analysis is based on a single CMB simulation for the 3-torus topology either for $L = 1.5$ or for $L = 4.0$. However, the CMB simulations require Gaussian random initial conditions leading to a statistical ensemble

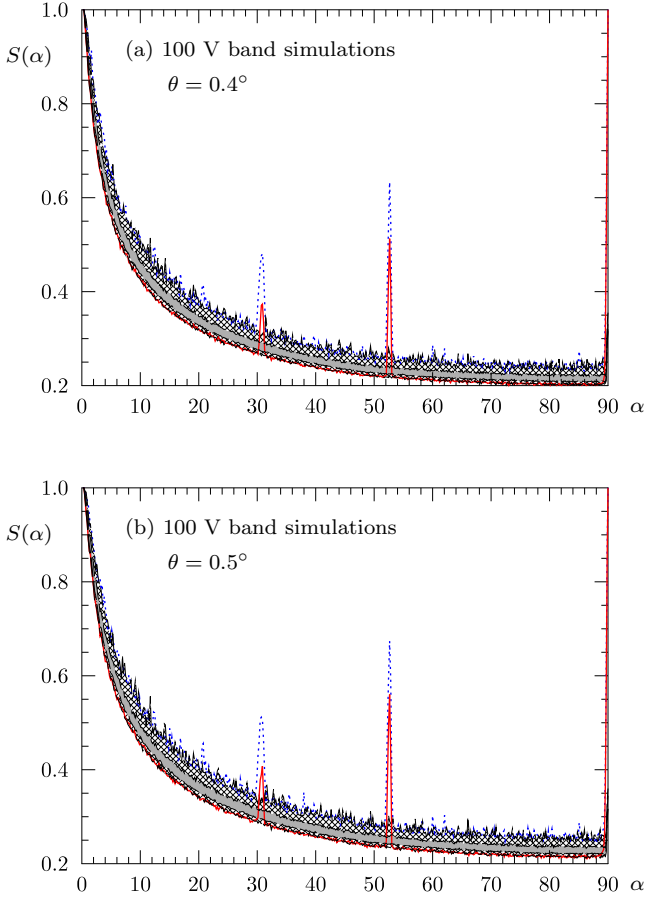


Figure 9. The CITS correlation $S(\alpha)$ is calculated for 100 different 3-torus simulations with $L = 4.0$ using the beam profile and the detector noise of the V band. The CMB maps are smoothed using the parameters $\theta = 0.4^\circ$ (panel (a)) and $\theta = 0.5^\circ$ (panel (b)) and downgraded to $N_{\text{side}} = 256$. The blue dotted curve shows the maximum of $S(\alpha)$ taken over all 100 simulations. The red full curve shows the corresponding minimum and represents thus the worst case occurring in the 100 simulations. The shaded band encompasses all values of $S_{\text{bg}}(\alpha)$ occurring in the 100 simulations, while the grey band contains 66 percent of the $S_{\text{bg}}(\alpha)$ values around their median. This reveals the variation of $S(\alpha)$ with respect to the random initial conditions of the CMB simulations.

of CMB simulations belonging to a given topology of a fixed side length L . In order to address the question how this variability affects the CITS signature, an ensemble of 100 CMB simulations for the 3-torus with $L = 4.0$ is generated. This leads to 100 CMB maps where the beam profile $b_{V1}(l)$ and the detector noise of the V band is taken into account as described above. The results for the two smoothing parameters $\theta = 0.4^\circ$ and $\theta = 0.5^\circ$ are presented in figure 9. The dotted curve shows the largest CITS signature that occurs in the 100 simulations, while the full curve shows the worst case that is the minimum over the 100 CITS correlations $S(\alpha)$. Individual matched circle pairs can possess even lower values, but note that $S(\alpha)$ takes the maximum of the 6 pairs at $\alpha = 31.1^\circ$ and of the 3 pairs at $\alpha = 52.7^\circ$. A detailed analysis reveals that the smoothing parameter $\theta = 0.5^\circ$ yields marginally better peaks than the choice $\theta = 0.4^\circ$.

At radii α where no matched circle pair is nearby, the

correlations $S_{ij}(\alpha, \beta)$, see eq.(1), show (positive) correlations and (negative) anti-correlations with the same amplitude, so that the minimum of the anti-correlations, defined by

$$S_{\text{bg}}(\alpha) = \max_{i,j,\beta} (-S_{ij}(\alpha, \beta)) \quad , \quad (5)$$

is a measure of the background even at radii α where matched circle pairs do occur. Thus it quantifies the detection threshold. The figure 9 shows the distribution of $S_{\text{bg}}(\alpha)$ obtained from the 100 simulations as the shaded band. This distribution is asymmetric with a tail towards larger values, and the figure 9 also shows as the grey band the band which contains 66 percent of the values of $S_{\text{bg}}(\alpha)$ around their median.

One observes in figure 9 that the CITS signature of the six matched circle pairs at $\alpha = 31.1^\circ$ is only slightly above this background in the worst case simulation. Since the measurements contain residual foregrounds not taken into account by our simulations, which further deteriorate the signal, it seems that even the detection of matched circle pairs around $\alpha = 30^\circ$ cannot be assured. For larger ring radii α , see the signature at $\alpha = 52.7^\circ$ in figure 9, the situation is far better, and such matched circle pairs should be detected.

6 CITS SIGNAL FOR THE W AND V BANDS USING MASKS

The noise is not the only problem for the CITS signature, since foreground sources dominate the CMB in some parts of the sky so that the CMB signal cannot be reliably reconstructed. The way out found in the literature consists of masking the problematic sky regions in the CMB map and replacing the temperature values by those of the ILC map. Here, we do not use the pixels which are too severely contaminated by foregrounds and compute the CITS correlation only with those pixels which are lying outside the KQ75 and KQ85 masks provided by the WMAP team (Bennett et al. 2012). Thereby arises the problem that the values of the CITS correlation cannot be compared for circles having the same radius α , since the correlations are computed from a different number of pixels depending on the orientation of the circles with respect to the mask. In a given HEALPix resolution N_{side} , a circle of radius α has the ring index n_{ring} in the RING scheme (Górski et al. 2005) of the HEALPix map, i.e. $n_{\text{ring}} = n_{\text{ring}}(\alpha)$. Define the number n_{eff} as the number of pixels that are used for the computation of the CITS correlation, that is $n_{\text{eff}} \leq n_{\text{eff}}^{\text{max}} = 4 \min(n_{\text{ring}}, N_{\text{side}})$ for $n_{\text{ring}} \leq 2N_{\text{side}}$ with equality for the case that the mask does not affect any pixel on the ring. The correlation $S(\alpha)$ is then analysed on the two-dimensional grid n_{eff} versus n_{ring} .

According to the results of the preceding sections, the foreground reduced V and W band maps (Bennett et al. 2012) are expanded in the resolution $N_{\text{side}} = 512$ with respect to a_{lm} and then are smoothed according to eq.(4). This yields the CMB maps which are analysed in the following subjected to the KQ75 or KQ85 mask.

We analyse the CMB maps with the resolution $N_{\text{side}} = 256$ for the smoothing parameters $\theta = 0.4^\circ$ and $\theta = 0.5^\circ$ by computing the CITS correlation S as a function of n_{ring} and n_{eff} . We do not find a pronounced peak in the data which could be interpreted as a signal for a matched circle pair.

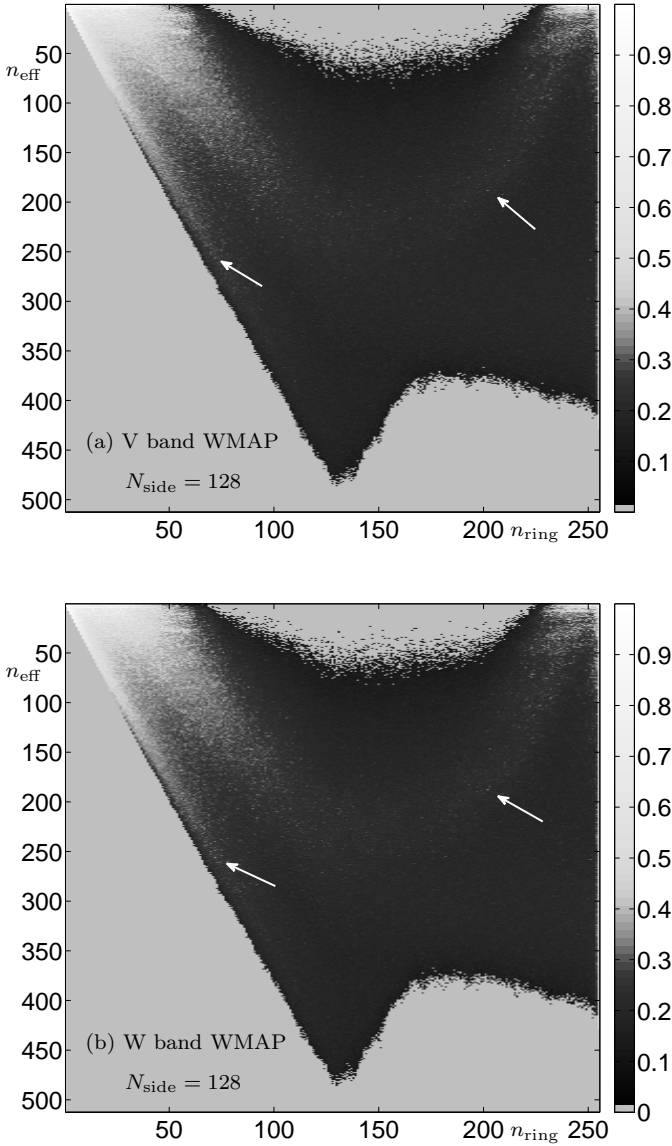


Figure 10. The CITS correlation S is computed for the V and W bands of the WMAP data using the resolution $N_{\text{side}} = 128$ as described in the text. The maps are smoothed to 0.5° and subjected to the KQ75 mask. The value of S encoded by brightness is shown as a function of n_{ring} and n_{eff} . Two interesting values are marked by arrows.

Although our tests with the topological simulations discussed in the previous sections suggests otherwise, we nevertheless searched in the lower resolution $N_{\text{side}} = 128$ after peaks. This differs from the search in the $N_{\text{side}} = 256$ maps by putting the average of four $N_{\text{side}} = 256$ pixels into one $N_{\text{side}} = 128$ pixel. By this additional averaging the detector noise is suppressed more than necessary according to our simulations. However, a possible residual foreground signal on small scales would also be smoothed out thereby reducing its contribution to the m -weighted circle signature defined in eq. (1). The figures 10 and 11 present the results for the CITS search in the $N_{\text{side}} = 128$ maps. In figure 10 the value of the CITS correlation is encoded by brightness. As already discussed, the horizontal axis n_{ring} corresponds to the radius α of the circle in the $N_{\text{side}} = 128$ resolution,

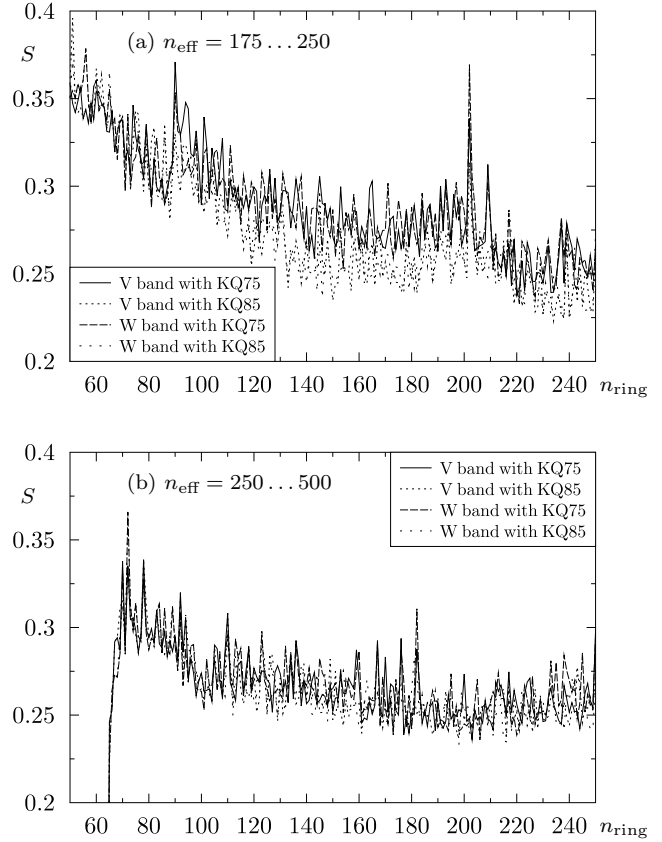


Figure 11. The CITS correlation $S(\alpha)$ shown in figure 10 is shown as a one-dimensional plot by taking the maximum of S over the stripe $n_{\text{eff}} \in [175, 250]$ in panel (a) and over the stripe $n_{\text{eff}} \in [250, 500]$ in panel (b). The peak at $n_{\text{ring}} = 202$ visible in panel (a) is marked by the right arrow in figure 10. The left arrow corresponds to the peak at $n_{\text{ring}} = 72$ seen in panel (b).

while the vertical axis over n_{eff} separates the CITS values with respect to the number of pixels on which its calculation is based. Towards smaller values of n_{eff} , the CITS value and correspondingly the brightness increases, in general, because a lower number of pixels enhances the probability of a large correlation by chance. A pronounced peak occurs at $n_{\text{ring}} = 202$ corresponding to $\alpha = 73.7^\circ$ and $n_{\text{eff}} = 188$. Its position is marked by an arrow in figure 10. A further peak at the position $n_{\text{ring}} = 72$ corresponding to a smaller ring with $\alpha = 26.6^\circ$ and $n_{\text{eff}} = 256$ is also marked. Although CITS values belonging to different values of n_{eff} cannot be strictly compared due to their different significance, we nevertheless combine two stripes with $n_{\text{eff}} \in [175, 250]$ and $n_{\text{eff}} \in [250, 500]$ by taking the maximum in the given n_{eff} interval for a fixed value of n_{ring} . The results are plotted in figure 11 for both stripes for the V and W band maps subjected to the KQ75 and KQ85 masks. Panel (a) reveals the pronounced peak at $n_{\text{ring}} = 202$. The signal is visible in all 4 cases shown in the figure. A further peak in panel (a) at $n_{\text{ring}} = 90$ emerges only by using the KQ75 mask and is absent using the KQ85 mask. The decrease in the CITS correlation is thus caused by pixels close to the boundary of the KQ75 mask. This case demonstrates that a few additional pixels can destroy a CITS signal. The peak at $n_{\text{ring}} = 72$

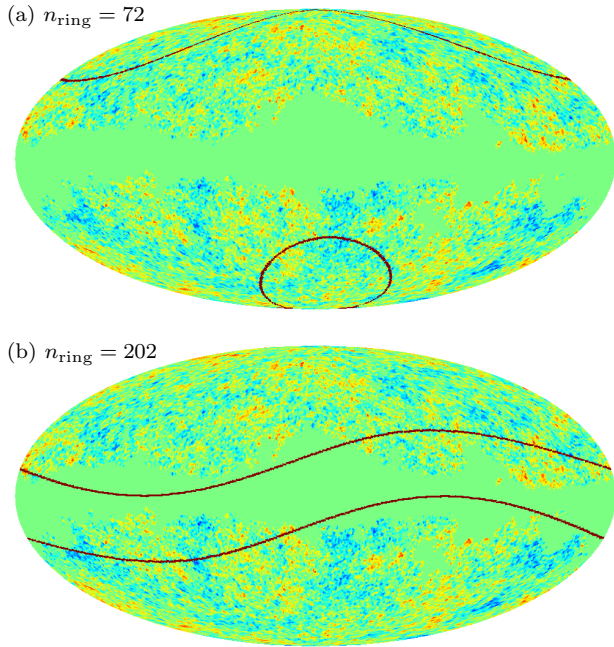


Figure 12. The W band temperature fluctuations subjected to the KQ75 mask are shown together with the position of the circle pair with $n_{\text{ring}} = 72$ (radius $\alpha = 26.6^\circ$) in panel (a) and with $n_{\text{ring}} = 202$ (radius $\alpha = 73.7^\circ$) in panel (b).

shown in panel (b) is more clearly seen in the W band data and is independent of the mask.

It is instructive to discuss the position of the circle pair on the CMB map. The large circle pair with $n_{\text{ring}} = 202$ lies in the neighbourhood of the galactic plane as figure 12(b) shows. This is the reason why large parts of this circle pair are excluded by the mask. In addition, this location bears the risk that many pixels used in the computation of the CITS correlation contain significant amounts of foreground contributions. The situation is more favourable in the case of the smaller circle pair with $n_{\text{ring}} = 72$ shown in figure 12(a). This pair is far away from the galactic plane and most pixels are taken into account. At $n_{\text{ring}} = 72$ one has $n_{\text{eff}}^{\text{max}} = 288$ which is close to $n_{\text{eff}} = 256$ found for this circle pair. On the other hand, the simulations of the preceding sections demonstrate that a circle pair with such a small radius is at the detection threshold.

The CITS signatures in the resolution $N_{\text{side}} = 128$ at $n_{\text{ring}} = 72$ and $n_{\text{ring}} = 202$ are probably generated by chance. This is suggested by a comparison with the results in the resolution $N_{\text{side}} = 256$ where these circle pairs reveal no unusual high correlation values. Furthermore, we add the V and W band maps after correcting for their different beam profiles. After smoothing the summation map with $\theta = 0.5^\circ$, it is downgraded to $N_{\text{side}} = 256$. The maximum of the correlation S with $n_{\text{eff}} \geq 300$ is plotted in figure 13 as the full curve, where the KQ85 mask is used. The values of n_{ring} for $N_{\text{side}} = 256$ are twice that of $N_{\text{side}} = 128$ for the same radii α . So peaks around $n_{\text{ring}} = 144$ and $n_{\text{ring}} = 404$ would be expected from the $N_{\text{side}} = 128$ results. Although a peak at $n_{\text{ring}} = 140$ appears, it has nothing to do with that in the $N_{\text{side}} = 128$ resolution, since its circle pair has a different orientation. Furthermore, this peak is absent if the KQ75

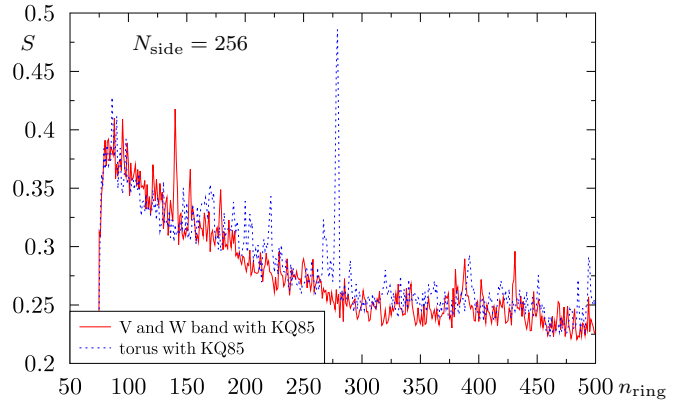


Figure 13. The full curve shows the CITS correlation S obtained from the addition of the V and W band CMB maps, while the dotted curve belongs to a torus simulation having a side length $L = 4.0$. The maximum of S over $n_{\text{eff}} \geq 300$ is plotted. The resolution $N_{\text{side}} = 256$ together with the KQ85 mask and a smoothing with $\theta = 0.5^\circ$ is used.

mask is used. The figure 13 also shows as a dotted curve the CITS correlation for a torus model with $L = 4.0$ having circles at $\alpha = 31.1^\circ$ ($n_{\text{ring}} = 168$ for $N_{\text{side}} = 256$) and at $\alpha = 52.7^\circ$ ($n_{\text{ring}} = 279$ for $N_{\text{side}} = 256$). The large circles at $n_{\text{ring}} = 279$ are clearly revealed, while none of the six small circle pairs at $n_{\text{ring}} = 168$ leads to enhanced correlation values. The fact that the circle pairs at $\alpha = 31.1^\circ$ are not detected, suggests that the peak at $n_{\text{ring}} = 140$ corresponding to $\alpha = 25.8^\circ$ is produced by chance. Furthermore, this fact also shows that matched circle pairs should have radii larger than $\alpha = 30^\circ$ in order to be detectable with WMAP data.

7 SUMMARY AND DISCUSSION

The circles-in-the-sky (CITS) signature provides a test for a possible non-trivial topology, i.e. for a multi-connected space, of our Universe. The detection threshold of a matched circle pair depends on the radius α of the circle. In order to determine the detection threshold, accurate CMB maps are simulated for the 3-torus topology, and their CITS correlations are computed for various circumstances.

The CITS correlation is introduced in eqs. (1) and (2) in section 2. This topological detection measure is applied to a simulated 3-torus CMB map for a restricted search for back-to-back circle pairs. It turns out that for radii $\alpha \gtrsim 25^\circ$ the CITS signal is strong enough for a detection of matched circle pairs. Furthermore, it is found that the highest correlation values are not found on the matched circles, but rather for neighbouring circles having slightly smaller radii. This effect is the more pronounced, the smaller the radii of the matched circle pairs are.

The experiments provide CMB maps in which the resolution is determined by the size of the pixels. Section 3 investigates the question how an additional Gaussian smoothing of the CMB data can enhance the detection probability for a matched circle pair. The amplitude of the CITS signal is compared with the detection threshold for several CMB simulations with different HEALPix resolutions N_{side}

and different Gaussian smoothing parameters θ , see eq. (3). This analysis leads to the conclusion that for $N_{\text{side}} = 256$ a smoothing parameter of $\theta = 0.4^\circ$ is preferable if the pixels contain the clean CMB signal. But for $N_{\text{side}} = 512$ one should prefer a smaller smoothing parameter θ in order to detect also matched circle pairs with smaller radii. Experimentally, such clean sky maps are not available because of detector noise and residual foregrounds.

Before these problems are addressed, we turn in section 4 to the question how sharp the peaks are which belong to genuine matched circle pairs. This determines the resolution of the search grid N_{grid} whose coordinates are used as possible circle centres for which the CITS correlation is computed. It is demonstrated that for a smoothing of $\theta = 0.4^\circ$ several matched circle pairs get missed at $N_{\text{grid}} = 128$ while using $N_{\text{side}} = 512$ for the CMB map. Although one can find matched circle pairs at $N_{\text{grid}} = 128$, one cannot exclude matched circle pairs if no circle pairs are found at this search grid resolution.

In sections 2 to 4 only general properties are studied without reference to a specific experiment. In section 5, however, CMB maps for the 3-torus topology are generated which take the noise properties of the V and W band channels of the WMAP satellite into account. The CITS correlation for a CMB map having the quality corresponding to the WMAP 9yr observations is computed in the $N_{\text{side}} = 512$ resolution. It turns out that CITS signal of the matched circle pairs is either absent or very faint which demonstrates that the noise is too severe in order to search directly in the original V and W band maps for a topological signature. This result is further substantiated by smoothing the $N_{\text{side}} = 512$ map using the parameters $\theta = 0.4^\circ$ and $\theta = 0.5^\circ$. These additionally smoothed $N_{\text{side}} = 512$ maps reveal the CITS peaks at the positions of the matched circle pairs. Such a smoothing is necessary for a sufficient suppression of noise. Since the above conclusions are based on a single CMB simulation, a set of 100 CMB maps is generated for the 3-torus topology with side length $L = 4$. Their 100 CITS correlations reveal the variability with respect to the Gaussian random initial conditions which determine how the eigenmodes are weighted. As shown in figure 9, the variability of the height of the CITS peaks at circle radii around $\alpha \simeq 30^\circ$ is so important that some matched circle pairs are at the detection limit. Around $\alpha \simeq 50^\circ$ the variability is of the same order, but the detection probability is not affected due to the more pronounced peaks.

Section 6 addresses as a further complication the residual foregrounds which can be so severe that it is advisable to mask the unsafe regions. As a consequence the CITS correlation can only be computed from the unmasked fraction of the circle leading to a statistical significance depending on the number n_{eff} of pixels used for the computation of the CITS correlation. The search for a CITS signature in the foreground reduced V and W band maps with $N_{\text{side}} = 256$ and $\theta = 0.4^\circ$ or $\theta = 0.5^\circ$ subjected to the KQ75 or KQ85 mask yields a negative result. Although the results obtained from our simulation would not advise to use the $N_{\text{side}} = 128$ resolution in a CITS search, we nevertheless carry out the $N_{\text{side}} = 128$ search and find some interesting peaks. A peak emerges from the background at the large circle radius $\alpha = 73.7^\circ$ as seen in figures 10 and 11(a). The corresponding circle pair lies, however, as seen

in figure 12(b), very close to the galactic plane. Since one expects the largest residual foregrounds close to the galactic plane, the suspicion arises that the signal might be spuriously generated by residual foregrounds. However, if one accepts such an argument, the reverse argument that these very residual foregrounds can also destroy a true CITS signal, have to be accepted in the same way. Furthermore, since so many pixels are masked in this circle pair, the high CITS correlation can also be produced by chance. A second interesting peak in the CITS correlation belongs to a circle radius $\alpha = 26.6^\circ$, which is also probably generated by chance as our simulations show. On the other hand, this circle pair is far from the galactic plane, and few pixels are masked and the residual foregrounds are less important. As demonstrated in section 6, the six circle pairs at $\alpha = 31.1^\circ$ in the $L = 4.0$ torus topology are not detected by using the quality of the WMAP data, which shows that matched circle pairs have to be larger than at least $\alpha = 30^\circ$ in order to be detectable. We are thus eagerly awaiting new more accurate data in order to see, whether the CITS peaks will withstand or prove to be a spurious result. Even if these CITS signatures will not endure, a multi-connected space can possess circle pairs that are not back-to-back and these are not considered in this paper. Examples for topologies with such generic matched circle pairs are provided by the half-turn space E_2 (Aurich and Lustig 2011) and by spherical double-action manifolds (Aurich and Lustig 2012b,a). These spaces would require an extended search for generic matched circle pairs.

ACKNOWLEDGMENTS

HEALPix [healpix.jpl.nasa.gov] (Górski et al. 2005) and the WMAP data from the LAMBDA website (lambda.gsfc.nasa.gov) were used in this work.

REFERENCES

- Aurich, R., Janzer, H. S., Lustig, S., and Steiner, F. (2008). Do we Live in a "Small Universe"? *Class. Quantum Grav.*, 25:125006.
- Aurich, R. and Lustig, S. (2011). Cosmic microwave anisotropies in an inhomogeneous compact flat universe. *Class. Quantum Grav.*, 28:085017.
- Aurich, R. and Lustig, S. (2012a). Cosmic topology of polyhedral double-action manifolds. *Class. Quantum Grav.*, 29:235028.
- Aurich, R. and Lustig, S. (2012b). Cosmic topology of prism double-action manifolds. *Class. Quantum Grav.*, 29:215005.
- Aurich, R., Lustig, S., and Steiner, F. (2006). The circles-in-the-sky signature for three spherical universes. *Mon. Not. R. Astron. Soc.*, 369:240–248.
- Bennett, C. L., Larson, D., Weiland, J. L., Jarosik, N., Hinshaw, G., Odegard, N., Smith, K. M., Hill, R. S., Gold, B., Halpern, M., Komatsu, E., Nolte, M. R., Page, L., Spergel, D. N., Wollack, E., Dunkley, J., Kogut, A., Limon, M., Meyer, S. S., Tucker, G. S., and Wright, E. L. (2012). Nine-Year Wilkinson Microwave Anisotropy

- Probe (WMAP) Observations: Final Maps and Results. *arXiv:1212.5225 [astro-ph.CO]*.
- Bielewicz, P. and Banday, A. J. (2011). Constraints on the topology of the Universe derived from the 7-yr WMAP data. *Mon. Not. R. Astron. Soc.*, 412:2104–2110.
- Cornish, N. J., Spergel, D. N., and Starkman, G. D. (1998). Circles in the sky: finding topology with the microwave background radiation. *Class. Quantum Grav.*, 15:2657–2670.
- Cornish, N. J., Spergel, D. N., Starkman, G. D., and Komatsu, E. (2004). Constraining the Topology of the Universe. *Phys. Rev. Lett.*, 92(20):201302–1–4.
- Fujii, H. and Yoshii, Y. (2011). An improved cosmic crystallography method to detect holonomies in flat spaces. *Astron. & Astrophys.*, 529:A121.
- Górski, K. M., Hivon, E., Banday, A. J., Wandelt, B. D., Hansen, F. K., Reinecke, M., and Bartelmann, M. (2005). HEALPix: A Framework for High-Resolution Discretization and Fast Analysis of Data Distributed on the Sphere. *Astrophys. J.*, 622:759–771. HEALPix web-site: <http://healpix.jpl.nasa.gov/>.
- Jarosik, N., Bennett, C. L., Dunkley, J., Gold, B., Greason, M. R., Halpern, M., Hill, R. S., Hinshaw, G., Kogut, A., Komatsu, E., Larson, D., Limon, M., Meyer, S. S., Nolte, M. R., Odegard, N., Page, L., Smith, K. M., Spergel, D. N., Tucker, G. S., Weiland, J. L., Wollack, E., and Wright, E. L. (2011). Seven-Year Wilkinson Microwave Anisotropy Probe (WMAP) Observations: Sky Maps, Systematic Errors, and Basic Results. *Astrophys. J. Supp.*, 192:14.
- Key, J. S., Cornish, N. J., Spergel, D. N., and Starkman, G. D. (2007). Extending the WMAP bound on the size of the Universe. *Phys. Rev. D*, 75(8):084034.
- Lachièze-Rey, M. and Luminet, J.-P. (1995). Cosmic topology. *Physics Report*, 254:135–214.
- Levin, J. (2002). Topology and the cosmic microwave background. *Physics Report*, 365:251–333.
- Luminet, J.-P. (2008). The Shape and Topology of the Universe. In *Proceedings of the conference "Tessellations: The world a jigsaw", Leyden (Netherlands), March 2006*.
- Luminet, J.-P. and Roukema, B. F. (1999). Topology of the Universe: Theory and Observation. In *NATO ASIC Proc. 541: Theoretical and Observational Cosmology*, page 117.
- Mota, B., Rebouças, M. J., and Tavakol, R. (2010). Circles-in-the-sky searches and observable cosmic topology in a flat universe. *Phys. Rev. D*, 81:103516.
- Mota, B., Rebouças, M. J., and Tavakol, R. (2011). What can the detection of a single pair of circles-in-the-sky tell us about the geometry and topology of the Universe? *Phys. Rev. D*, 84:083507.
- Rathaus, B., Ben-David, A., and Itzhaki, N. (2013). Orbifold Line Topology and the Cosmic Microwave Background. *arXiv:1302.7161 [astro-ph.CO]*.
- Rebouças, M. J. and Gomero, G. I. (2004). Cosmic Topology: a Brief Overview. *Braz. J. Phys.*, 34:1358–1366.
- Riazuelo, A., Caillerie, S., Lachièze-Rey, M., Lehoucq, R., and Luminet, J.-P. (2006). Constraining Cosmic Topology with CMB Polarization. *arXiv:astro-ph/0601433*.
- Roukema, B. F., France, M. J., Kazimierczak, T. A., and Buchert, T. (2013). Deep redshift topological lensing: strategies for the T^3 candidate. *arXiv:1302.4425 [astro-ph.CO]*.
- Roukema, B. F., Lew, B., Cechowska, M., Marecki, A., and Bajtlik, S. (2004). A hint of Poincaré dodecahedral topology in the WMAP first year sky map. *Astron. & Astrophys.*, 423:821–831.
- Vaudrevange, P. M., Starkman, G. D., Cornish, N. J., and Spergel, D. N. (2012). Constraints on the Topology of the Universe: Extension to General Geometries. *Phys. Rev. D*, 86:083526.